Flexoelectricity-driven toroidal polarisation topology in liquid-matter helielectrics

Jidan Yang[1]†, Yu Zou[1]†, Jinxing Li[1], Mingjun Huang[1,2]*, Satoshi Aya[1,2]*

[1] South China Advanced Institute for Soft Matter Science and Technology (AISMST), School of Emergent Soft Matter, South China University of Technology, China.
[2] Guangdong Provincial Key Laboratory of Functional and Intelligent Hybrid Materials and Devices, South China University of Technology, Guangzhou 510640, China.

#1. Supplementary Figures 1-15

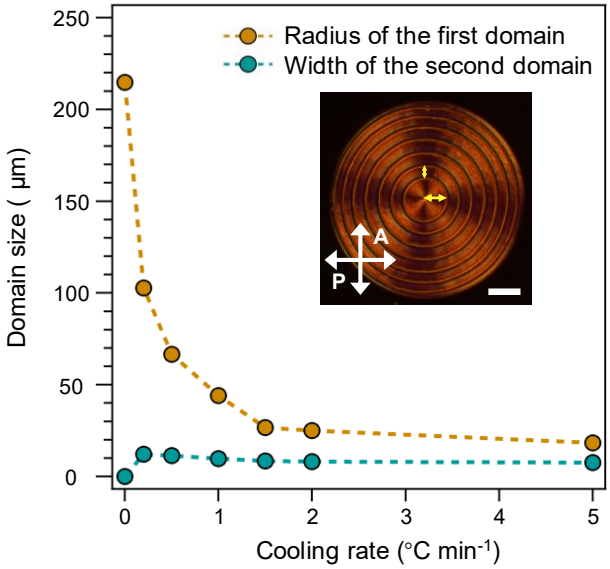

Supplementary Fig. 1. The radius or width of the first (orange dot) and second domain (green dot) as a function of the cooling rate for an RM-OC_2/S1 mixture with 0.3 wt% S1. Bright yellow double arrows in the PLM image show how we measure the radius or width. The thickness of the homemade cell is 3.2 μm. Scale bar, 30 μm.

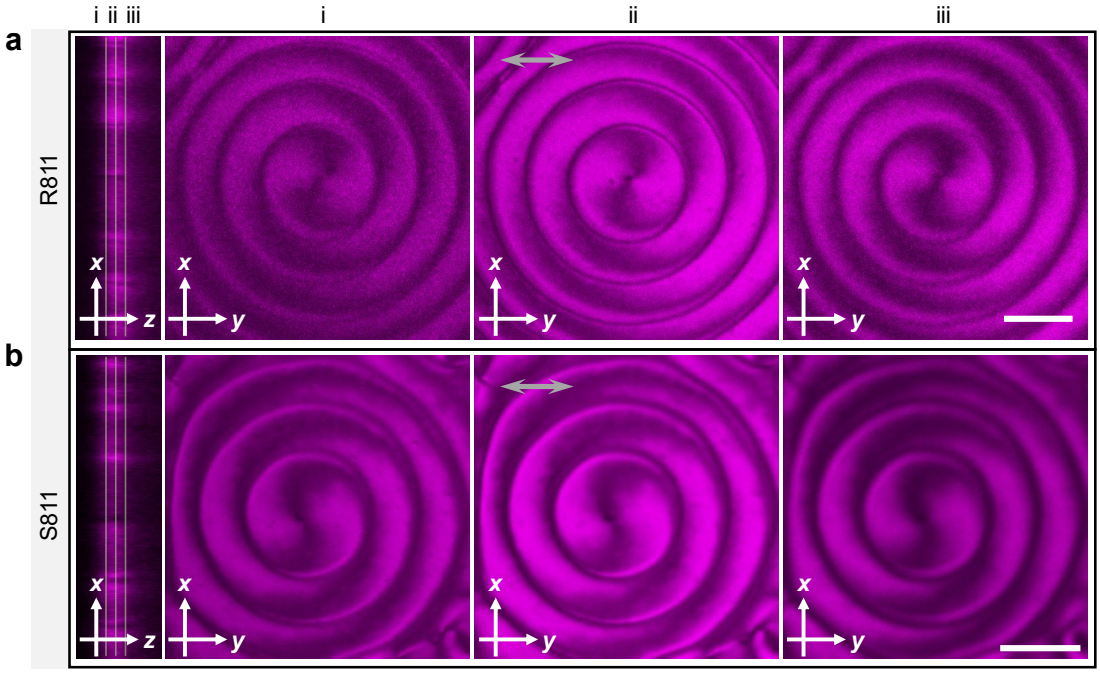

Supplementary Fig. 2. FCPM images of toroidal polarisation topology with the opposite handedness. The grey double arrow represents the linear polarisation of the incident light. **a**,**b**, The cross-sectional FCPM images of the toroidal polarisation topology by mixing RM-OC_2 with R811(a) and S811(b). *xy*- and *xz*-cross-sectional images are visualized by a linear polarisation at three different positions. Scale bars, 20 μm. The concentration of R811 and S811 is 0.5 wt %. The sample thickness is 3.2 μm.

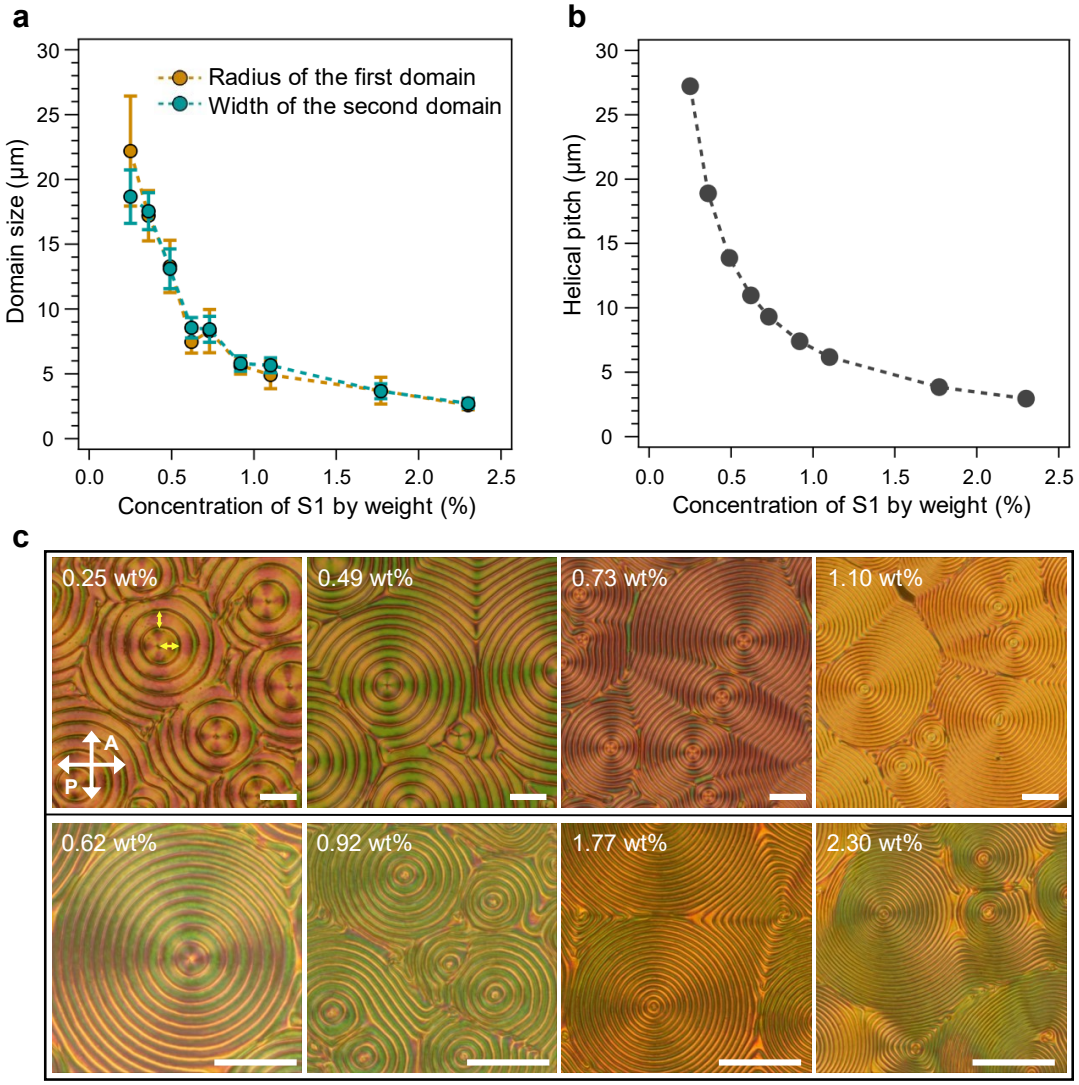

Supplementary Fig. 3. a, The radius of the first domain (orange solid dots) and width of the second domain (green solid dots) as a function of the concentration of the chiral dopant, S1. The error bars show the standard deviations of the mean radius of the first domain and the mean width of the second domain. **b**, The black dots represent the helical pitch as a function of the concentration of S1. **c**, PLM images of the random generation of the toroidal polarisation structures in RM-OC_2/S1 mixtures at different concentrations of S1. The thickness of the homemade cell is 3.2 μm. Scale bars, 50 μm.

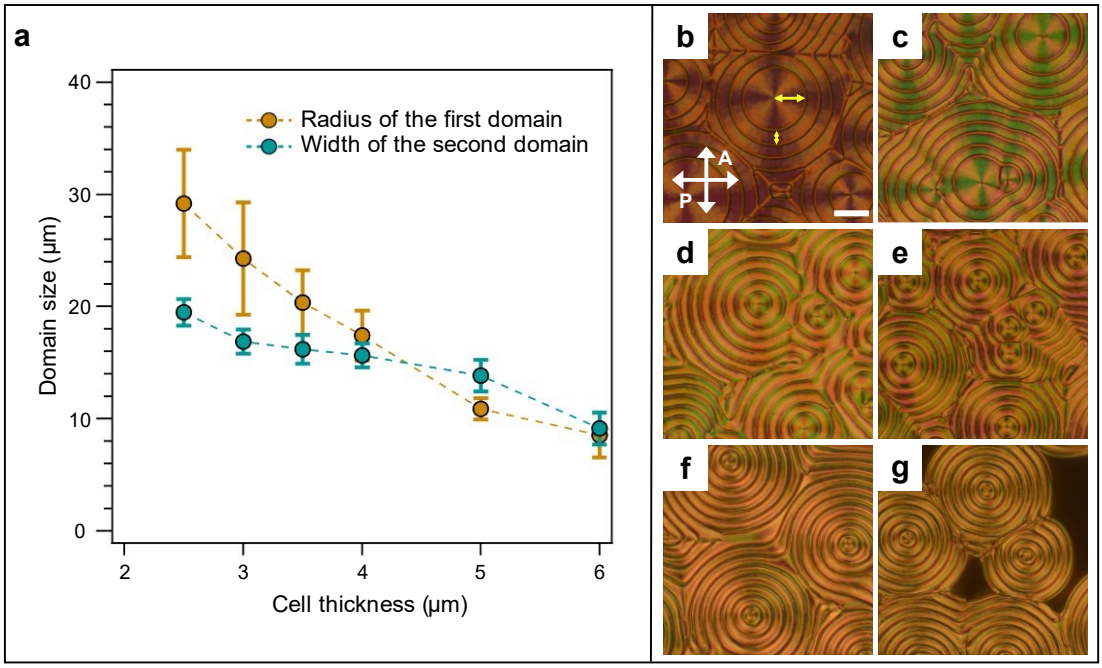

Supplementary Fig. 4. a, the radius or width of the first (orange dot) and second domain (green dot) as a function of the cell thickness for an RM-OC_2/S1 mixture with 0.49 wt% S1. The error bars show the standard deviations of the mean radius or mean width of the first domain and second domain. **b-g**, PLM images of the random generation of toroidal polarisation structures for RM-OC_2/S1 mixture in the thickness of 2 μm (b), 3 μm (c), 3.5 μm (d), 4 μm (e), 5 μm (f), and 6 μm (g). Bright yellow double arrows in the PLM image show how we measure the radius or width. Scale bar, 50 μm.

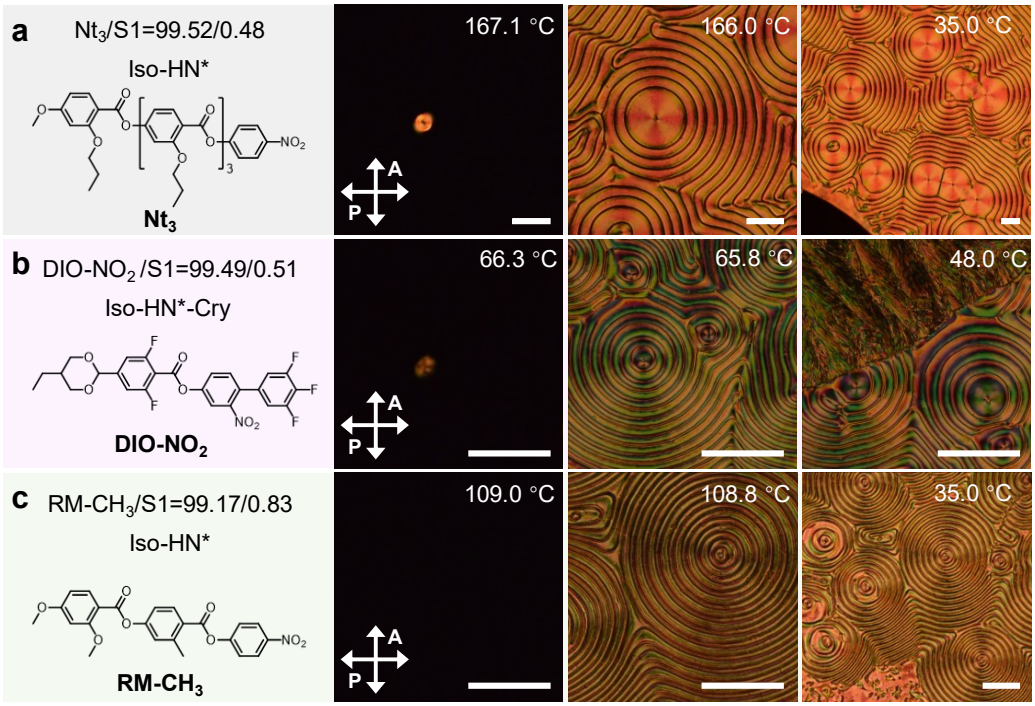

Supplementary Fig. 5. The representative PLM texture evolution of Nt_3/S1 = 99.52/0.48 (a), DIO-NO_2/S1 = 99.49/0.51 (b) and RM-CH_3/S1 = 99.17/0.83 (c) under crossed polarizers. The thickness of the homemade cell is 5 μm. Scale bars, 100 μm.

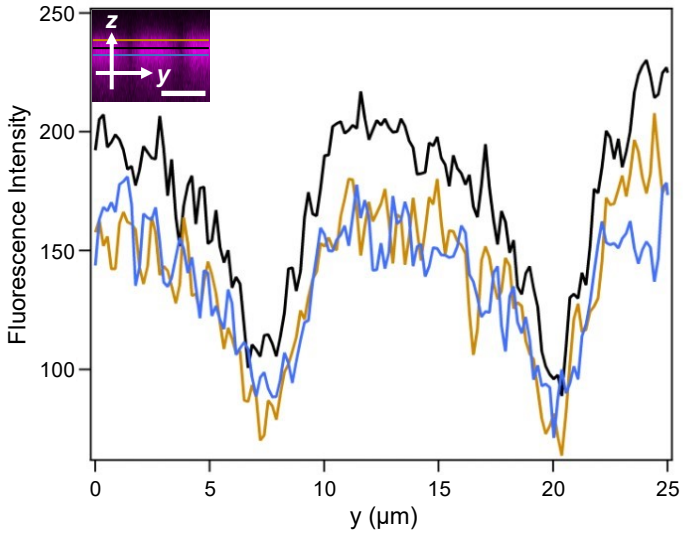

Supplementary Fig. 6. The diagram showing the intensity profile of the FCPM image. The *yz*-cross-section of the experimental FCPM image with two sharp dark domain walls was inserted in the diagram. Scale bar, 10 μm. The black line represents the intensity profile along the path in the center area of the FCPM image. The blue and yellow lines represent the intensity profile along the path in the non-center area of the FCPM image.

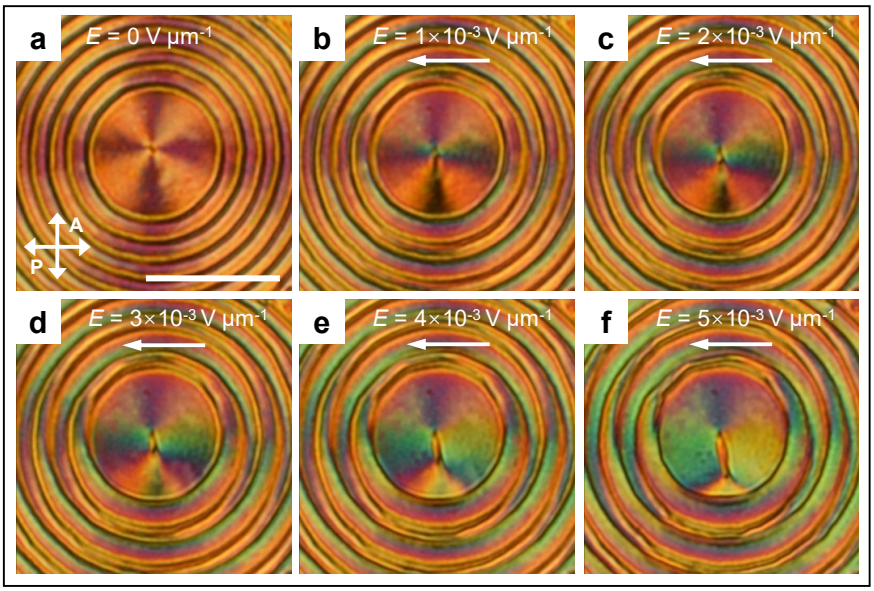

Supplementary Fig. 7. The PLM observation showing the evolution of the toroidal polarisation topology with the continuously increasing electric field. The direction of the electric field is indicated by white arrows. Scale bar, 50 μm.

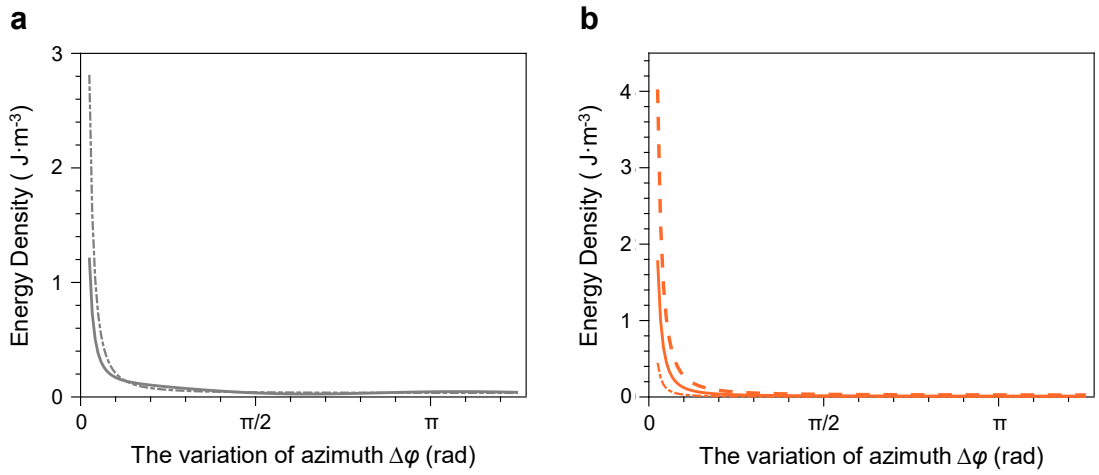

Supplementary Fig. 8. Numerically calculated free energy densities of the elastic and polarisation gradient terms for an HN* droplet as the function of $\Delta\varphi$. **a,** nematic elastic free energy curves in two cases: $\widetilde{K} = 0$ (grey solid line) and $\widetilde{K} \neq 0$ (grey dot-dash line). **b,** Free energy density of the polarisation gradient term with different polarisation strength: $P_0 = 2$ μC·cm^{-2} (orange long-dash line), $P_0 = 4$ μC·cm^{-2} (orange solid line) and $P_0 = 6$ μC·cm^{-2} (orange dot-dash line). Here, k is set to be $\pi/12$ μm^{-1}. Additional parameters involved in the calculations can be found in the Methods.

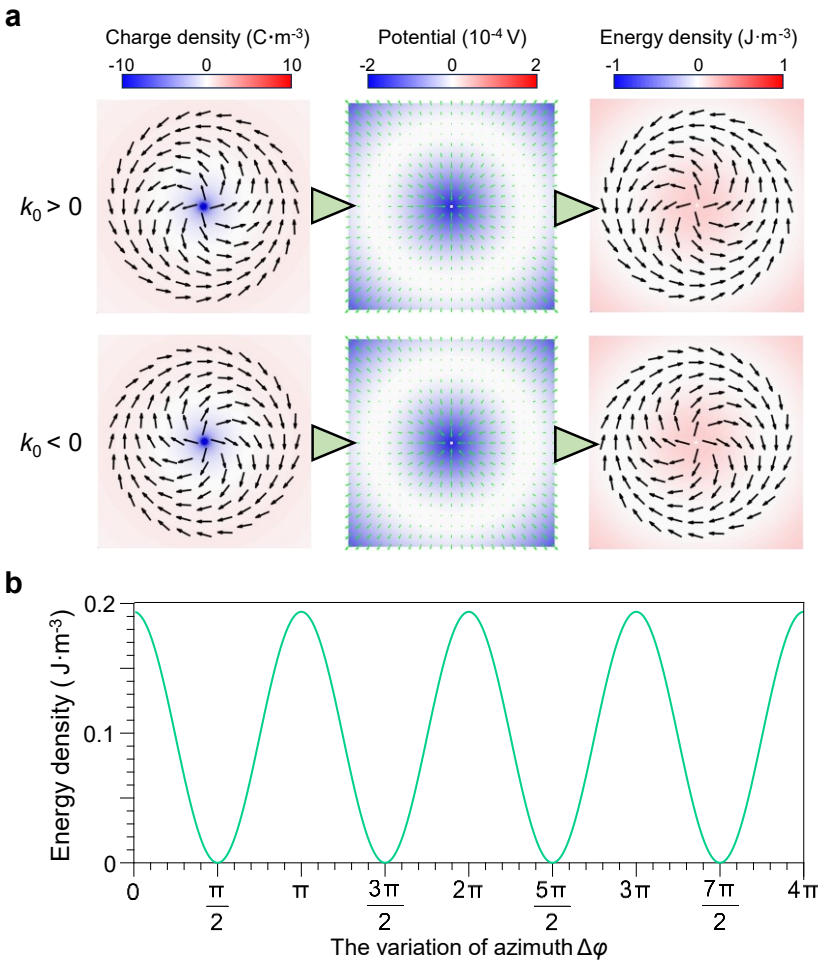

Supplementary Fig. 9. Numerical calculations for the space charge effect. **a,** the spatial distributions of the induced space charge, potential and the energy density are shown. **b,** The free energy density of the depolarisation charge effect as a function of $\Delta\varphi$. Here, β is set to be 2×10^{-4}. k is set to be $\pi/12$ μm^{-1}. Additional parameters used for the calculation can be found in Methods.

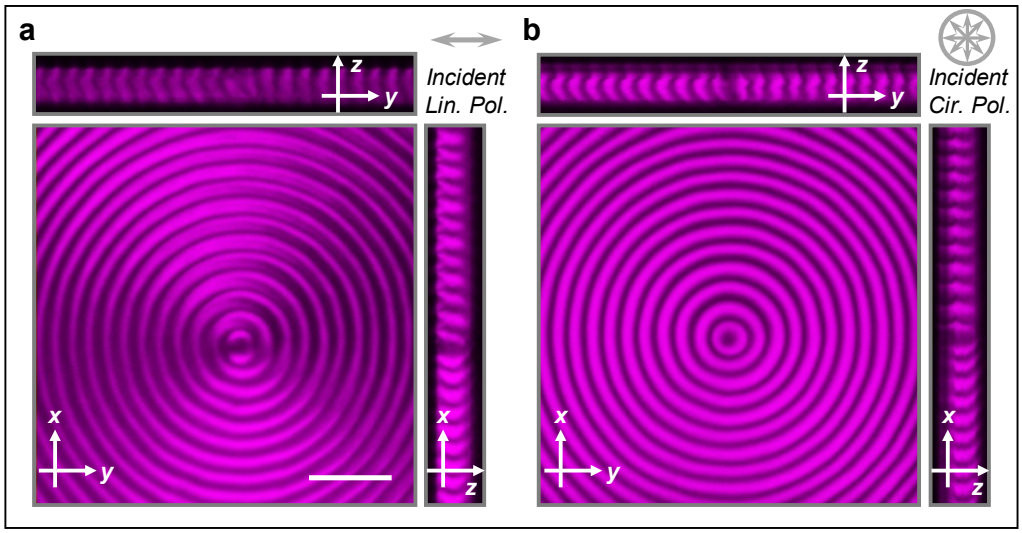

Supplementary Fig. 10. Representative FCPM cross-sectional images of the HN* droplet in the RM-OC_2/S1=99.51/0.49 mixture doped with Nile Red (c = 0.05wt%). The image is taken by using a linearly polarised light (a) and a circularly polarised light (b) in a 6 μm LC cell. Scale bar, 20μm.

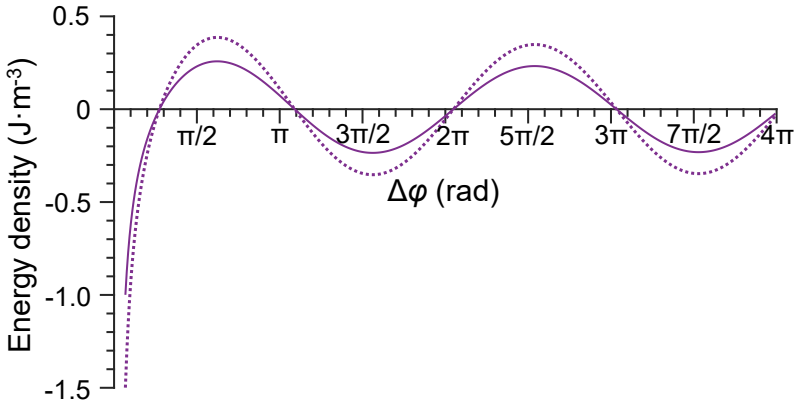

Supplementary Fig. 11. Numerically calculation the flexoelectric energy density f_{flexo} as the function of $\Delta\varphi$ under two different parameter conditions: $\gamma = 2 \times 10^{-4}$ V and $\gamma = 3 \times 10^{-4}$ V. The variation of γ does not affect the distributions of zeros and extremes of the function. k is set to be $\pi/12$ μm^{-1}. Additional parameters used for the calculation can be found in Methods.

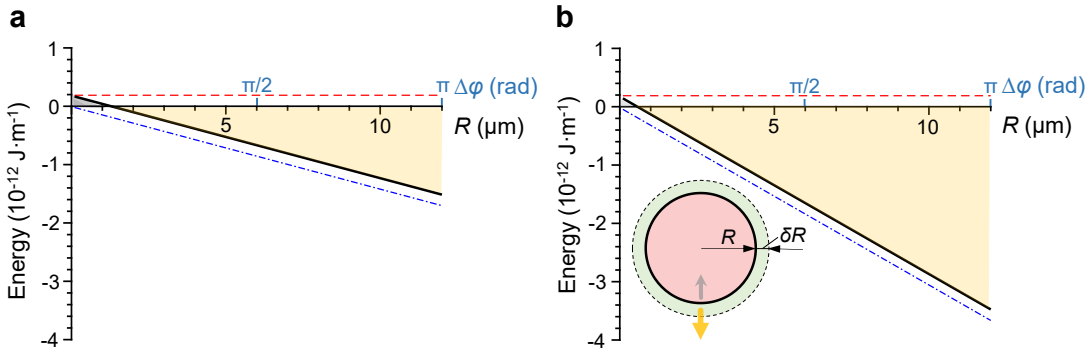

Supplementary Fig. 12. The free energy variations upon the growth of a polar droplet from a radius R to a radius $R + \delta R$. With the same effective surface force $\sigma = 3 \times 10^{-7}$ N·m^{-1}, the free energy change of the droplet is shown for two different Landau energy conditions: **a,** $\tau_1 = -10^3$ J·m·C^{-2} and $\tau_2 = 5.56 \times 10^5$ J·m^5·C^{-4}, so the equilibrium polarisation strength is $P_0 = 3$ μC·cm^{-2}; **b,** $\tau_1 = -10^3$ J·m·C^{-2} and $\tau_2 = 2.6 \times 10^{-5}$ J·m^5·C^{-4}, so the equilibrium polarisation strength is $P_0 = 4.4$ μC·cm^{-2}. The critical radius for generating polar droplets increases with decreasing polarity. It is seen that the polar droplet is harder to be produced when the polarity of system is small (a). Additional parameters used for the calculation can be found in Methods.

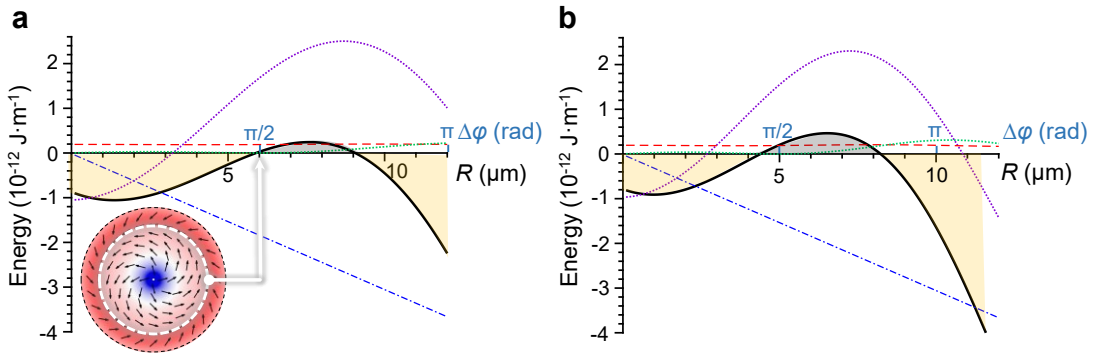

Supplementary Fig. 13. The free energy variations upon the growth of a HN* droplet from a radius R to a radius $R + \delta R$. The flexoelectric effect dominates here. Here two values are set for the variation rate of the azimuthal angle along the radial direction: **a,** $k = \pi/12$; **b,** $k = \pi/10$. In both cases, the first crossover of δE from negative to positive values occurs near $\Delta\varphi \approx \pi/2$. Other parameters involved in the calculations are set as same as Fig. 5e used.

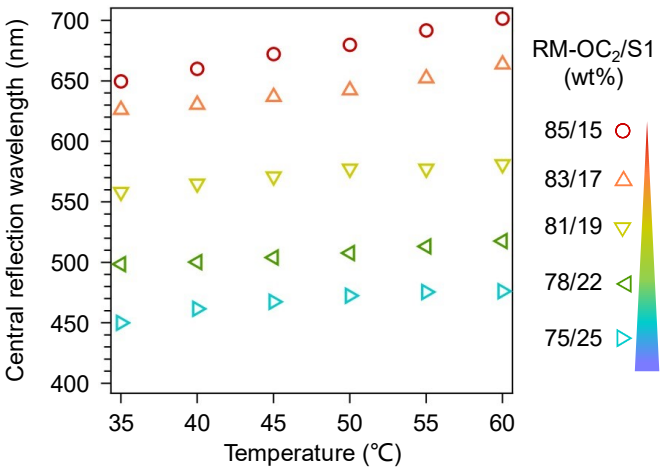

Supplementary Fig. 14. The temperature dependencies of the mean visible-light reflection peaks for RM-OC_2/S1 mixtures. The reflection experiments are made in 5-μm LC cells.

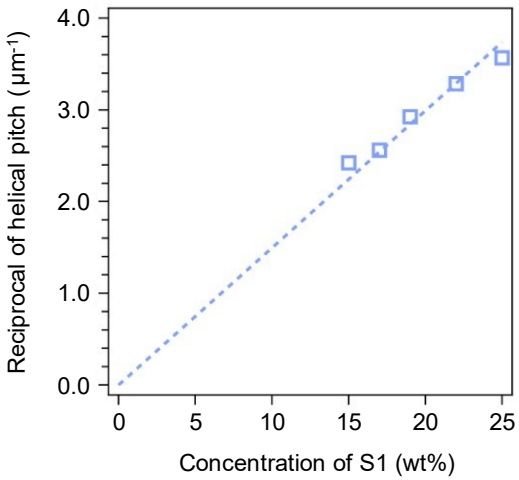

Supplementary Fig. 15. The reciprocal of the helical pitch as a function of the concentration of chiral dopant, S1, in RM-OC_2.

#2. Materials and Methods

Materials

(R)-2-Octyl 4-[4-(Hexyloxy)benzoyloxy]benzoate (R811) and (S)-2-Octyl 4-[4-(Hexyloxy)benzoyloxy]benzoate (S811) are obtained from Sigma-Aldrich and the other molecules are synthesized according to our previous papers[1-4]. All the used molecular structures are drawn as below.

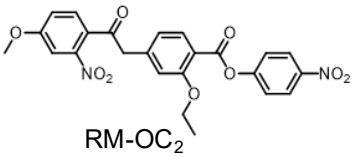

RM-OC_2

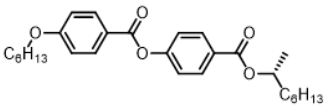

R811

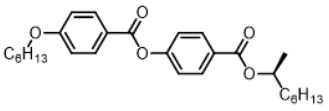

S811

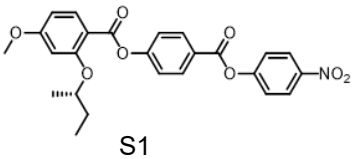

S1

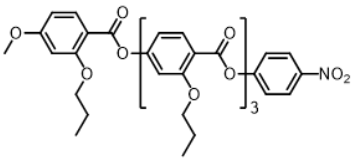

Nt_3

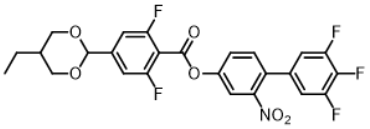

DIO-NO_2

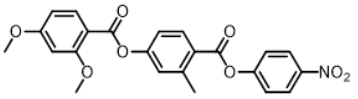

RM-CH_3

#3. Supplementary Discussions

Supplementary Discussion 1. Free-energy calculation

The toroidal polarisation topology with periodically-banded domains in the HN* droplets is modelled by inserting domain walls (DWs) into a virtual polarisation texture. The polarisation (or director) rotates continuously along the droplet radial direction. To mathematically represent the latter polarisation fields, we use the common form of the director $\mathbf{n} = (\cos\varphi\cos\delta, \sin\varphi\cos\delta, \sin\delta)$ and set $\mathbf{P} = P_0\mathbf{n}$. φ and δ are the azimuthal and elevation angles for the director, respectively. Due to the constant fluorescence intensity in the *xy*-plane in FCPM images captured with circularly polarised light (Fig. 3a), it is clear that there is little elevation angle of director field. Therefore, we set $\delta = 0$. The azimuthal angle φ vary linearly along the radial direction and takes the form:

$$\varphi = \theta + kr + b. \tag{S1}$$

θ and r are the polar angles in polar coordinates and distance from the droplet center, respectively. k is the variation rate of the azimuthal angle along the radial direction. b is the initial azimuth angle for the directors near the droplet center. A two-dimensional (2D) model for a virtual topological texture accompanied by a continuous rotation of the polarisation along the radial direction without DWs is described as:

$$n_x = \frac{x\cos\left(k\sqrt{x^2+y^2}+b\right) - y\sin\left(k\sqrt{x^2+y^2}+b\right)}{\sqrt{x^2+y^2}}, \tag{S2}$$

$$n_y = \frac{y\cos\left(k\sqrt{x^2+y^2}+b\right) + x\sin\left(k\sqrt{x^2+y^2}+b\right)}{\sqrt{x^2+y^2}}, \tag{S3}$$

$$n_z = 0. \tag{S4}$$

Next, we discuss the free energy terms in the HN* state. As the nematic continuum theory describes, LC deformation consumes three types of elastic free energy, which can be expressed by the classical Oseen-Frank form, i.e.,

$$f_{\text{elast}} = \frac{1}{2}K_{11}(\nabla\cdot\mathbf{n})^2 + \frac{1}{2}K_{22}[\mathbf{n}\cdot(\nabla\times\mathbf{n}) + q]^2 + \frac{1}{2}K_{33}[\mathbf{n}\times(\nabla\times\mathbf{n})]^2, \tag{S5}$$

K_{11}, K_{22}, and K_{33} are the elastic constants for splay, twist, and bend deformation, respectively. q is the wavenumber. The polar free energy terms consist of

$$f_{\text{polar}} = \frac{1}{2}h(\nabla\mathbf{P})^2 - \frac{1}{2}\mathbf{P}\cdot\mathbf{E}_{\text{b}} - \gamma\mathbf{n}(\nabla\cdot\mathbf{n})\cdot\mathbf{P}, \tag{S6}$$

$$f_{\text{Landau}} = \frac{1}{2}\tau_1\mathbf{P}^2 + \frac{1}{2}\tau_2\mathbf{P}^4. \tag{S7}$$

The first term of f_{polar} is the polarisation gradient with the coefficient h and $(\nabla\mathbf{P})^2 = \sum_{i,j}\left(\partial_i P_j\right)^2 (i,j \in x,y,z)$. The second term of f_{polar} comes from the depolarisation charge

effect and $\mathbf{E}_\mathrm{b}$ is the depolarised field. The last term originates from the flexoelectric effect, which tends to generate the directional splay in the polar phases (Fig. 1a). γ is the flexoelectric coefficient. f_Landau is the Landau energy density with the coefficients τ_1 and τ_2. τ_1 is related to the temperature for Iso-HN* transition, i.e., $\tau_1 = \alpha(T - T_0)$. It determines the equilibrium order parameter of the polarisation $\mathbf{P}$. The sign of τ_2 determines the stability of the polar phase. For $\tau_2 > 0$, the system tends to stabilise the polar state and undergoes a second-order phase transition. The equilibrium polarisation strength in the HN* state is described by $P_0 = \sqrt{-\tau_1/2\tau_2}$.

We insert Eqs. (S2 − S4) into Eq. (S5 − S7) to calculate the free energy density. The elastic term reads:

$$\begin{aligned} f_\mathrm{elast} &= \frac{1}{2}K_{11}(\nabla\cdot\mathbf{n})^2 + \frac{1}{2}K_{22}[\mathbf{n}\cdot(\nabla\times\mathbf{n}) + q]^2 + \frac{1}{2}K_{33}[\mathbf{n}\times(\nabla\times\mathbf{n})]^2 \\ &= \frac{K_{22}q^2}{2} + \frac{\overline{K}(1+k^2r^2)}{2r^2} \\ &+ \frac{\widetilde{K}}{2r^2}[(k^2r^2-1)\cos(2kr+2b) + 2kr\sin(2kr+2b)]. \end{aligned} \tag{S8}$$

$\overline{K}$ represents the average of K_{11} and K_{33}, i.e., $\overline{K} = (K_{33} + K_{11})/2$. $\widetilde{K}$ describes the elastic anisotropy, i.e., $\widetilde{K} = (K_{33} - K_{11})/2$. The absolute total variation of the azimuthal angle from the droplet center is defined by $\Delta\varphi = |kr|$. Supplementary Fig. 8a shows the numerical calculation of f_e as a function of $\Delta\varphi$ in both cases of with (the blue dotted line) and without (the red solid line) the elastic anisotropy. There is no a significant difference in the free energy variations, thus whether including the elastic anisotropy in the calculation does not essentially modify the stability of the polar structures. For simplicity, we set $K_{11} = K_{22} = K_{33} = K$ in the following analytical calculations. Under this circumstance, the nematic elastic free energy density reads:

$$f_\mathrm{elast} = \frac{K}{2}\left[\frac{1}{r^2} + k^2 + q^2\right]. \tag{S9}$$

The polarisation gradient term which penalizes the distortion of the polarisation field is:

$$f_\mathrm{grad} = \frac{h{P_0}^2}{2r^2}(1 + k^2r^2). \tag{S10}$$

Similar to the elastic free energy term, the polarisation gradient free energy density also decreases as the distance r increases (Supplementary Fig. 8b). The depolarisation charge is induced by the divergence of the polarisation field. The induced charge is expressed as:

$$\begin{aligned} \sigma_\mathrm{b} &= -\beta(\nabla\cdot\mathbf{P}) \\ &= \beta P_0\left[k\sin(\Delta\varphi + b) - \frac{\cos(\Delta\varphi + b)}{r}\right]. \end{aligned} \tag{S11}$$

Because the accumulation of depolarisation charge is only related to the absolute value of k (Its

sign represents the handedness of the polarisation topology), kr is replaced by $\Delta\varphi$ in Eq. (S11). β is a dimensionless coefficient which relates to the ionic effects in the N_F system. As reported by Perera et al[5], there would be free ions that will screen out space charge in the N_F state, leading to the actual amount of space charge to be much lower than the theoretical prediction ($\int(\nabla\cdot\mathbf{P})\,dV$). With this in mind, we set a parameter $\beta \ll 1$ here (Methods). The spatial distribution of depolarisation charges is visualised in the left column of Supplementary Fig. 9a. By solving the Poisson equation, we obtain the depolarisation potential Φ and then determine the corresponding depolarisation field $\mathbf{E}_\mathrm{b} = \left(E_x, E_y\right)$ (the middle column of Supplementary Fig. 9a) as:

$$\nabla^2\Phi = -\frac{\sigma_\mathrm{b}}{\varepsilon} \Rightarrow \Phi = C_1 + C_2 \ln r + \frac{\beta P_0}{k\varepsilon}\sin(\Delta\varphi + b)\,, \tag{S12}$$

$$E_x = -\frac{\cos\theta}{\varepsilon}[C_2\varepsilon + \beta P_0 r\cos(\Delta\varphi + b)], \tag{S13}$$

$$E_y = -\frac{\sin\theta}{\varepsilon}[C_2\varepsilon + \beta P_0 r\cos(\Delta\varphi + b)]. \tag{S14}$$

C_1 and C_2 are the constants obtained by solving Poisson's equation. The unit of C_1 is V, which corresponds to a offset of the potential. The unit of C_2 is $\mathrm{V\cdot m^{-1}}$, corresponding to the local depolarisation field. ε is the effective dielectric constant for HN* LCs. In the presence of a depolarising field, the free energy density for the space charge is:

$$\begin{aligned} f_\mathrm{depol} &= -\frac{1}{2}\mathbf{P}\cdot\mathbf{E}_\mathrm{b} \\ &= \frac{P_0}{2}\cos(\Delta\varphi + b)\left[\frac{C_2}{r} + \frac{\beta P_0}{\varepsilon}\cos(\Delta\varphi + b)\right]. \end{aligned} \tag{S15}$$

Numerical calculation of f_depol as a function of r yields the free energy density mapping in the right column of Supplementary Fig. 9a. The value of f_depol oscillates along the radial direction, taking the local maximums at around $\Delta\varphi = m\pi$ (m is an integer) and local minimums at around $\Delta\varphi = (2m-1)\pi/2$ (Supplementary Fig. 9b). The flexoelectric term is:

$$\begin{aligned} f_\mathrm{flexo} &= -\gamma\mathbf{n}(\nabla\cdot\mathbf{n})\cdot\mathbf{P} \\ &= \gamma P_0\left[k\sin(kr + b) - \frac{\cos(kr + b)}{r}\right]. \end{aligned} \tag{S16}$$

Eq. (S16) indicates that f_flexo modulates along the radial direction, determined by the trigonometric functions fluctuating. By numerically calculating f_flexo as the function of $\Delta\varphi$ with different values of γ, we found that the variation of γ does not affect where f_flexo gets across zero and maximum (Supplementary Fig. 11). Therefore, when the azimuthal angle of the polarisation continuously rotates along the radial direction, it is inevitable to create a negatively-splayed region where $f_\mathrm{flexo} > 0$. This free-energy increase upon the HN* growth

hinders the system from further rotating the polarisation. Finally, the Landau energy density is a constant and reads:

$$f_{\text{Landau}} = \frac{1}{2}\tau_1 \mathbf{P}^2 + \frac{1}{2}\tau_2 \mathbf{P}^4 = \frac{1}{2}\left(\tau_1 {P_0}^2 + \tau_2 {P_0}^4\right). \quad \text{(S17)}$$

Since the equilibrium polarisation strength of the system is determined by the Landau coefficients, i.e., $P_0 = \sqrt{-\tau_1/2\tau_2}$, Eq. (S17) can also be written as $f_{\text{Landau}} = \tau_1 {P_0}^2/4$.

Supplementary Discussion 2. Energy conditions for droplet growth

Whether the nucleation and growth of a droplet nucleating from another phase would proceed is determined the competition between the additional surface energy and the free energy gain of the new phase (e.g., Fig. 5c). For HN* droplets, we consider both the apolar and polar contributions to the surface energy. The apolar surface energy corresponds to the normal tension (σ) between the Iso and HN* states. For a 2D HN* droplet with a radius of R, the apolar surface energy is calculated as $W_{\text{apolar}} = 2\sigma\pi R$. When the droplet grows to a radius of $R + \delta R$, the apolar surface energy increases to $\delta E_{\text{apolar}} = 2\sigma\pi\delta R$. The polar surface energy arises due to the surface charge generated by the finite angle between the tangent line on droplet's interface and the neighbouring polarization in the virtual polarization texture. This polar surface term is written as:

$$\sigma_{\text{polar}} = \beta_1(\mathbf{P}\cdot\mathbf{v})^2 = \beta_1 {P_0}^2 \cos^2(b + kr) \quad \text{(S18)}$$

$\mathbf{v}$ is the normal vector on the droplet's interface. β_1 is a coefficient related to the bound charge effect, i.e., $\beta_1 = \xi\beta/\varepsilon$. From Eq. (S18), one can see that the action range of σ_{polar} relates to the spatial scale of the order parameter $\mathbf{P}$. Thus, we introduce a length factor ξ into the coefficient β_1 and set it to be 100 nm which is as same as the mesh spacing in the numerical calculation. For a HN* droplet with a radius of R, the polar surface energy is calculated as $W_{\text{apolar}} = 2\pi\beta_2 {P_0}^2 R\cos^2(b + kR)$. The variation of W_{polar} caused by increasing the droplet radius from R to $R + \delta R$ can be calculated as

$$\begin{aligned}\delta E_{\text{polar}} &= 2\pi\beta_1 {P_0}^2\{(R+\delta R)\cos^2[b + k(R+\delta R)] - R\cos^2(b+kR)\} \\ &\approx 2\pi\beta_1 {P_0}^2 \delta R[\cos^2(b+kR) - kR\sin(2b+2kR)] \end{aligned} \quad \text{(S19)}$$

For the analytical solution, we ignore higher order infinitesimals (e.g., δR^2) and conduct the following approximations: $\sin(k\delta R) \sim k\delta R$ and $k(R+\delta R) \sim kR$. Therefore, the total surface energy variation by increasing the droplet radius from R to $R+\delta R$ is:

$$\delta E_{\text{surf}} \approx 2\pi\sigma\delta R + 2\pi\beta_1 {P_0}^2 \delta R[\cos^2(b+kR) - kR\sin(2b+2kR)]. \tag{S20}$$

On the other hand, the Landau energy in the polar phase favours the droplet growth. The Landau energy variation by increasing the droplet radius from R to $R+\delta R$ is:

$$\begin{aligned}\delta E_{\text{Landau}} &= \int_0^{2\pi}\int_R^{R+\delta R} f_{\text{Landau}} \cdot r\, dr d\theta \\ &= \frac{\pi\tau_1 {P_0}^2}{4}(2R\delta R + \delta R^2) \\ &\approx \frac{\pi}{2}\tau_1 {P_0}^2 R\delta R\end{aligned} \tag{S21}$$

Similarly, the space charge and flexoelectric terms reads:

$$\begin{aligned}\delta E_{\text{flexo}} &= \int_0^{2\pi}\int_R^{R+\delta R} f_{\text{flexo}} \cdot r\, dr d\theta \\ &= -2\pi\gamma P_0\{(R+\delta R)\cos[k(R+\delta R)+b] - R\cos(kR+b)\} \\ &\approx -2\pi\gamma P_0 \delta R\{\cos(kR+b) - kR\sin(kR+b)\}\end{aligned} \tag{S22}$$

$$\begin{aligned}\delta E_{\text{depol}} &= \int_0^{2\pi}\int_R^{R+\delta R} f_{\text{depol}} \cdot r\, dr d\theta \\ &= \frac{\pi\beta P_0}{8k^2\varepsilon}\left\{\begin{aligned}&\frac{16\varepsilon E_0 k}{\beta}\sin\frac{k\delta R}{2}\cos\left(b+kR+\frac{k\delta R}{2}\right)+ \\ &2P_0\left[\begin{aligned}&k(R+\delta R)\sin(2b+2kR+2k\delta R) - kR\sin(2b+2kR) \\ &+k^2\delta R^2 + 2k^2 R\delta R - \sin(k\delta R)\sin(2b+2kR+k\delta R)\end{aligned}\right]\end{aligned}\right\} \\ &\approx \frac{\pi\beta {P_0}^2\delta R}{2\varepsilon}\left[\frac{2\varepsilon C_2}{\beta P_0}\cos(b+kR) + R\right]\end{aligned} \tag{S23}$$

According to Eqs. (S20 − S23), we numerically calculated the energy variations of an HN* droplet increasing the radius from R to $R+\delta R$ based on the finite element method (Methods; Figs. 5c-f). Further, the total energy variation by increasing the droplet radius by δR in an HN* droplet with the virtual polarization texture is described as:

$$\begin{aligned}\delta E &= \delta E_{\text{surf}} + \delta E_{\text{Landau}} + \delta E_{\text{flexo}} + \delta E_{\text{depol}} \\ &\approx \left(2\pi\sigma + \frac{\pi\tau_1 {P_0}^2}{2}R\right)\delta R - 2\pi\gamma P_0\delta R[\cos(kR+b) - kR\sin(kR+b)] \\ &+ \frac{\pi {P_0}^2\delta R}{2}\left\{\frac{2C_2}{P_0}\cos(b+kR) + \frac{\beta}{\varepsilon}R + 4\beta_1[\cos^2(b+kR) - kR\sin(2b+2kR)]\right\}.\end{aligned} \tag{S24}$$

The continuous growth of the HN* droplets is energetically favourable when $\delta E < 0$ and unfavourable otherwise. We first consider the simplest case that the competition between the surface tension and Landau energy dictates whether the polar droplet would be stabilised (i.e., setting $\gamma = 0$ V, $\beta = 0$ and $C_2 = 0$ V). By numerically calculating Eq. (S24) as the function of R under different Landau coefficients (Supplementary Fig. 11), it is clear that larger polarity of system favours the formation of the polar droplet. When the depolarisation charge and flexoelectric effects cannot be ignored, the total energy variation δE changes its sign as the HN* droplet grows up. When the depolarisation charge effect dominates, the polar droplet with a continually rotating polarisation field becomes energetically unstable. When the flexoelectric effect dominates, the first crossover of δE from negative to positive occurs near $\Delta\varphi \approx \pi/2$. This is because the system is unlikely to allow the negatively-splayed polarisation field to exist as aforementioned. Further, we show that the position at which the crossover occurs is mainly related to the total variation in the azimuth angle $\Delta\varphi$ (Supplementary Fig. 12). As mentioned before, where the crossover and local maximum of f_{flexo} occur only depends on the polarisation's azimuthal angle. This rule also applies to the distribution of the local maximum of $\delta E_{\mathrm{flexo}}$ because they have similar mathematical forms (Eq. (S16) and Eq. (S22)). Therefore, under the dominance of the flexoelectric effect, some variations of other parameters (such as k and γ) only slightly modify the positions where the crossover of δE occurs. On the other hand, the depolarisation charge across DWs is minimised when the polarisation vectors on both sides of DWs are antiparallel. The prohibition of the depolarisation charge across DWs makes the polarisation parallel to DWs, thus tending to keep that the crossover of δE from negative to positive occurs at $\Delta\varphi \approx \pi/2$. When the energy scales for the depolarization charge and flexoelectric effects are comparable, the crossover of δE occurs at $\Delta\varphi \approx \pi/2$ as well. This is because the flexoelectric effect also plays a major role in the location of the DW. Therefore, the formation of the experimentally observed toroidal polarisation topology should be controlled by the flexoelectric effect. Considering the key competition caused only by the surface energy, Landau energy and flexoelectric energy, we also calculate the analytical solution of the critical radius R_{c} where DW is inserted according to Eq. (S24). Before the calculation, we set the parameters E_0 and β to be zero and made the following approximation in the context of $\Delta\varphi \in [\pi/8, 3\pi/4]$ based on Eq. (S24):

$$\cos\Delta\varphi - \Delta\varphi \sin\Delta\varphi \approx -1.85\Delta\varphi + 1.51. \tag{S25}$$

Then, the critical radius R_{c} is estimated as

$$R_{\mathrm{c}} \approx \frac{6\gamma P_0 - 4\sigma}{7.4k\gamma P_0 + \tau_1 {P_0}^2}. \tag{S26}$$

Clearly, R_c decreases as the surface tension σ increases. Taking the first order partial derivative of R_c with respect to γ, we obtained

$$\frac{\partial R_c}{\partial \gamma} = \frac{29.6k\sigma + 6\tau_1 {P_0}^2}{P_0(7.4k\gamma + \tau_1 P_0)^2}. \tag{S27}$$

Note that the Landau energy is much larger than the surface energy as described by Fig. 5c for the HN* system, so $29.6k\sigma + 6\tau_1 {P_0}^2 < 0$ applies to this case. Thus, we conclude that this critical radius also decreases as the flexoelectric coefficient γ increases ($\partial R_c/\partial \gamma < 0$). Indeed, when the variation of the azimuthal angle of the polarisation approaches $\pi/2$, both the surface tension and the flexoelectric effect tend to suppress the topology or droplet growth as discussed earlier.

#4. Supplementary Reference

1. Zhao, X.*et al.* Spontaneous helielectric nematic liquid crystals: Electric analog to helimagnets. *Proc. Natl. Acad. Sci. U. S. A.* **118**, e2111101118 (2021).

2. Yang, J.*et al.* Spontaneous electric-polarization topology in confined ferroelectric nematics. *Nat. Commun.* **13**, 7806 (2022).

3. Li, J.*et al.* How Far Can We Push the Rigid Oligomers/Polymers toward Ferroelectric Nematic Liquid Crystals? *J. Am. Chem. Soc.* **143**, 17857-17861 (2021).

4. Li, J.*et al.* General phase-structure relationship in polar rod-shaped liquid crystals: Importance of shape anisotropy and dipolar strength. *Giant* **11**, 100109 (2022).

5. Perera, K.*et al.* Ferroelectric nematic droplets in their isotropic melt. *Soft Matter* **19**, 347-354 (2023).